



Unmanned aerial vehicle inspection of the Placer River Trail Bridge through image-based 3D modelling

Ali Khaloo, David Lattanzi , Keith Cunningham, Rodney Dell'Andrea & Mark Riley

To cite this article: Ali Khaloo, David Lattanzi , Keith Cunningham, Rodney Dell'Andrea & Mark Riley (2017): Unmanned aerial vehicle inspection of the Placer River Trail Bridge through image-based 3D modelling, Structure and Infrastructure Engineering, DOI: [10.1080/15732479.2017.1330891](https://doi.org/10.1080/15732479.2017.1330891)

To link to this article: <http://dx.doi.org/10.1080/15732479.2017.1330891>



Published online: 30 May 2017.



Submit your article to this journal [↗](#)



View related articles [↗](#)



View Crossmark data [↗](#)



Unmanned aerial vehicle inspection of the Placer River Trail Bridge through image-based 3D modelling

Ali Khaloo^a, David Lattanzi^a , Keith Cunningham^b, Rodney Dell'Andrea^c and Mark Riley^d

^aDepartment of Civil, Environmental, and Infrastructure Engineering, George Mason University, Fairfax, VA, USA; ^bScenarios Network for Alaska & Arctic Planning, University of Alaska-Fairbanks, Fairbanks, AK, USA; ^cAlaska and Pacific Northwest Regions - Engineering, US Forest Service, Juneau, AK, USA; ^dR6 Data Resources Management, US Forest Service, Portland, OR, USA

ABSTRACT

Unmanned aerial vehicles (UAV) are now a viable option for augmenting bridge inspections. Utilising an integrated combination of a UAV and computer vision can decrease costs, expedite inspections and facilitate bridge access. Any such inspection must consider the design of the UAV, the choice of cameras, data acquisition, geometrical resolution, safety regulations and pilot protocols. The Placer River Trail Bridge in Alaska recently served as a test bed for a UAV inspection methodology that integrates these considerations. The end goal was to produce a three-dimensional (3D) model of the bridge using UAV-captured images and a hierarchical Dense Structure-from-Motion algorithm. To maximise the quality of the model and its benefits to inspectors, this goal guided UAV design and mission planning. The resulting inspection methodology integrates UAV design, data capture and data analysis together to provide an optimised 3D model. This model provides inspection documentation while enabling the monitoring of defects. The developed methodology is presented herein, as well as analyses of the 3D models. The results are compared against models generated through laser scanning. The findings demonstrate that the UAV inspection methodology provided superior 3D models with the accuracy to resolve defects and support the needs of infrastructure managers.

ARTICLE HISTORY

Received 6 October 2016

Revised 13 March 2017

Accepted 13 March 2017

KEYWORDS

Bridge inspection; robotics; computer vision; 3D modelling; light detection and ranging; photogrammetry; unmanned aerial vehicle; point clouds

1. Introduction

Inspecting and managing transportation infrastructure, considering the heavy usage of these systems, pose significant challenges to engineers and owners. The National Bridge Inspection Standards (NBIS) mandate that road bridges carrying passenger vehicles must receive a routine inspection every two years (Ryan, Mann, Chill, & Ott, 2012). The specifics of the inspection requirements vary based on structure type, materials and location, among many parameters. In most cases, these inspections are primarily visual and require hands-on observations in order to check for loose and broken hardware, spalling, corrosion, crushing, delamination, insect damage and a multitude of other maintenance and safety issues (Jahanshahi, Kelly, Masri, & Sukhatme, 2009).

Meeting these requirements often involves the use of specialised heavy machinery, such as an under-bridge inspection truck, to gain access. This equipment requires hiring trained operators and often necessitates the shutdown, or partial shutdown, of traffic on a bridge during an inspection. In addition, significant variability in the observations of inspection teams can make this process highly subjective and qualitative. Given the two-year inspection interval, the cost and transportation of the inspection equipment and the impacts to the travelling public, there is a need for improved inspection techniques that minimise these

costs and impacts while improving the quality and consistency of collected data. As recently investigated by McGuire, Atadero, Clevenger, and Ozbek (2016), utilising modern techniques such as building information modelling (BIM) and 3D virtual reconstruction can facilitate more efficient and cost-effective management of bridge inventories.

The National Forest Road System, managed and maintained by the U.S. Forest Service (USFS), has 612,000 km (380,000 miles) of roads and 7500 bridges across the country, many of which require NBIS inspection. Aside from the challenges endemic to the typical bridge inspection process, many USFS-maintained bridges are in remote locations or are access-restricted due to seasonal weather. This can pose a particular challenge when both heavy inspection equipments are required and bridge site access is limited. As a result, the USFS is currently exploring the use of unmanned aerial vehicles (UAV) to augment conventional NBIS inspections procedures.

UAV address many of the challenges of the bridge inspection process, as their portability and manoeuvrability can mitigate the need for heavy inspection equipment. As such, they present an ideal inspection tool for use in rugged and difficult to access locations. UAVs are capable of carrying a variety of active and passive sensing instruments, including near infrared (NIR), shortwave infrared (SWIR), thermal infrared (TIR), light detection and ranging (LIDAR), microwave systems, radar and optical

imagery (Colomina & Molina, 2014). In most cases, UAV carry consumer-grade digital cameras as inspection payloads. They are an intuitive and obvious payload choice, given the visual nature of NBIS inspections. Ultimately, the challenge is in developing a UAV, mission plan and data analysis approach that are integrated into a process that maximises the effectiveness of UAV in satisfying NBIS protocols.

1.1. Prior work in UAV infrastructure inspection

UAV systems have been utilised as remote-sensing platforms for diverse engineering purposes and for a more detailed discussion of the breadth of these applications the reader is referred to the review studies of Pajares (2015) and Colomina and Molina (2014). Recently, researchers have studied using UAV as a data acquisition platform for a wide variety of civil infrastructure applications in order to overcome accessibility issues in large and complex environments. Siebert and Teizer (2014) presented an autonomous approach that leverages UAV to generate 3D mapping data for civil site surveys of construction environments. Díaz-Vilariño, González-Jorge, Martínez-Sánchez, Bueno, and Arias (2016) employed Structure-from-Motion (SfM) techniques for the 3D reconstruction of aerial imagery in order to evaluate roadway runoff. UAV have seen use in disaster assessments and recovery efforts, in tandem with other robotic systems to provide situational awareness, and for performing large-scale aerial assessments (Murphy et al., 2008). Fernandez Galarreta, Kerle, and Gerke (2015) also considered UAV in the context of post-disaster structural damage assessment, generating and analysing image-based 3D models captured by the UAV.

With regard to structural condition assessment, early studies tended to use single or double rotor UAV platforms to carry inspection payloads, and focused on how to provide a stable inspection platform (Metni & Hamel, 2007). Recent advancements in multirotor systems have made them the preferred choice, as these systems tend to be more manoeuvrable, offer increased stability and are highly customisable. Of late, the focus has been on the analysis of the data collected by UAV. Researchers have studied how to use UAV to collect data from sensor networks embedded in a bridge, as well as how to use digital image information for condition assessments (Mascareñas, Flynn, Farrar, Park, & Todd, 2009). As presented by Roca, Lagüela, Díaz-Vilariño, Armesto, and Arias (2013), a Microsoft Kinect sensor was mounted on a UAV for 3D geometric data acquisition of building façades and roofs. However, lack of local point density within the generated point clouds and the poor performance of the Kinect in capturing data from reflective materials and in varied lighting conditions limit the capabilities of this approach.

In the work by Ellenberg, Kontsos, Moon, and Bartoli (2016), two-dimensional (2D) imagery collected by UAV was used to measure deformations in simulated damage scenarios through a series of computer vision algorithms. In the study by Sánchez-Aparicio, Riveiro, González-Aguilera, and Ramos (2014), a hybrid point cloud was generated from both LIDAR and photogrammetry techniques to characterise historic buildings, using a UAV for image data collection. Rodriguez-Gonzalvez, Gonzalez-Aguilera, Lopez-Jimenez, and Picon-Cabrera (2014) captured images from a UAV and used them to reconstruct 3D models of complex electrical substations. However, the scalability

and efficiency of their method were not investigated in terms of generating large-scale 3D point clouds.

1.2. Focus of this study

The Placer River Bridge, located within the Chugach National Forest (Girdwood, Alaska, U.S.A.) on Alaska's Kenai Peninsula, was chosen as a test site for the prototyping and testing of a new UAV bridge inspection methodology to support USFS bridge inspection practice. As a long-span water crossing, this bridge poses many of the accessibility challenges common to USFS bridges that must meet the NBIS inspection provisions.

This paper presents the results of the UAV inspection of this 85 m long clear-span timber truss bridge that took place over the course of two days. The major desired deliverable for the research team was a highly dense and multi-scale photorealistic as-built 3D computer model of the bridge. Multi-scale in this context refers to a model's ability to resolve structural details at a wide range of spatial scales, from representations of localised deficiencies to the global geometric configuration. The hierarchical Dense Structure-from-Motion (DSfM) process first explored in Khaloo and Lattanzi (2016) was adapted for use in conjunction with a UAV imaging system. The demands of this process were used as the basis for both mission planning and UAV design as part of a data-driven inspection methodology. The UAV was specifically designed to serve as a suitable data collection platform, with enhanced payload capacity and stability to acquire the necessary image quality and resolution.

Mission planning (flight and data acquisition) was done according to the specifications needed for the detailed 3D model generation, which requires high overlap imagery and multiple low-altitude flights to achieve small ground sample distances (GSD). By utilising this integrated approach, it was feasible to reconstruct a large-scale 3D scene of almost 1.5 billion points while maintaining the resolution needed to represent small details and flaws. It is also the first time, to the authors' best knowledge, that a multi-scale photogrammetric 3D scene reconstruction technique has been used to generate a highly accurate and dense 3D point cloud of a large-scale bridge using UAV-acquired images. The integrated inspection framework, multi-scale imaging and reconstruction methodology, and the comparative analysis with LIDAR results are the primary contributions of this paper.

Details of mission planning and logistics are first presented, followed by a presentation of the purpose-designed inspection UAV. The approach used to generate the 3D point cloud models is then presented. A qualitative and quantitative analysis of the collected data-sets in comparison with both traditional field measurements and LIDAR models are presented and discussed as well. The paper concludes with a discussion of the key conclusions and avenues for future study.

2. Project planning and logistics

The Placer River Bridge, completed in July 2013 and located near the Spencer Glacier, is only accessible via the Alaska Railroad followed by a short trail hike (Figure 1). The bridge is managed for pedestrian use. The bridge spans 85 m (280 feet) over the



Figure 1. The Placer River Bridge.



Figure 2. UAV Hexacopter platform used for acquiring data.

Table 1. Hexacopter technical specifications.

Parameter	Value
Weight (without payload)	6.48 kg (14.3 lbs)
Aircraft height	31.75 cm (12.5 inch)
Aircraft diameter (motor-to-motor)	80.01 cm (31.5 inch)
Motor type	Brushless DC
Motor power (each)	2/3 hp
Propeller size	38.1 cm (15 inch)
Battery time and size	LiPo-350 Wh
Launch and recovery method	Vertical Takeoff and Landing (VTOL)
Maximum takeoff weight	8 kg (17.637 lbs)
Maximum hover time	18 min
Maximum speed	32 km/h (20 mph)
Maximum range (line of sight)	1.61 km (1 mile)
Maximum payload weight	1.5 kg (3.31 lbs)
Maximum wind speed	32 km/h (20 mph)

Placer River, making it the longest clear-span timber truss bridge in North America.

As a water crossing, the underside of the bridge deck at mid-span is inaccessible and cannot be inspected from the ground. Furthermore, the remote location and access restrictions preclude the use of heavy inspection equipment. All of these factors made the Placer River Bridge an ideal test site for a UAV bridge inspection.

2.1. Project goals

The project's ultimate goal was to gain a greater understanding of the nature and quality of UAV-captured imaging necessary to supplement conventional bridge inspections, a potential step towards low-cost, high-frequency condition assessment. Digital images and videos captured via UAV can be disorienting and difficult to review, as studied in Lattanzi and Miller (2015). Ideally, by converting the images into a photorealistic 3D model of the bridge, inspectors can perform a visual NBIS structural integrity evaluation on a computer through a high-fidelity 3D virtual environment without the safety risks and time constraints of the field environment.

To generate these models, an adaptation of the DSfM process was employed. Essentially, the approach requires capturing hundreds or thousands of high-resolution digital images with a high degree of overlap between those images. Using a series of computer vision processes described later, a 3D point cloud of the structure is generated. Given sufficient accuracy and resolution, these models can be employed to measure deflections, changes in bridge cambers or other deformations and distortions of truss members. But in order to create the high-resolution models necessary to reconstruct bridge details, the captured images must maximise resolution and minimise image degradations due to UAV camera movements. The process also requires a specialised image capture plan that had direct impacts on mission day planning and UAV piloting.

2.2. UAV design

Satisfying the project goals required designing and constructing a UAV capable of carrying two cameras, with one on a gimbal mount for positional control and stability, and one that faced upwards, in order to capture all facets of the bridge. The UAV also needed to provide maximum stability in variable weather conditions, as the project team was concerned that wind vortex shedding might degrade collected images due to motion blur. The chosen aircraft was developed at the University of Alaska at Fairbanks (UAF) by Northern Embedded Solutions, which works closely with UAF on aircraft and sensor customisation. The platform was designed based on the DJI S800 airframe. The six-rotor hexacopter is called the 'Ptarmigan', named after the state bird of Alaska (Figure 2).

The airframe is made of carbon fibre, with retractable landing gear. Its design permitted a relatively large payload (approximately 1.5 kg) to be fitted beneath the rotor-lifting plane. Two cameras were mounted on the UAV. A Sony NEX-7 (24.3-megapixel resolution, CMOS sensor) camera with a 50 mm *f*/1.8 lens was mounted on a gimbal mount. A GoPro Hero 3 (11-megapixel resolution) camera was mounted on rails extending from beneath the aircraft into a position above the rotor-lift-plane to enable upwards imaging. The battery was also fitted on an adjustable rail mechanism beneath the lifting-plane so that the centre of gravity could be adjusted. This allowed for compensation of the effect of repositioning the camera on the aircraft's centre of gravity by adjusting the position of battery. The battery provided an endurance of 20–25 min, adequate for the line of sight flights and data collection missions. More information on the UAV system is listed in Table 1.



Figure 3. Sample images captured using the UAV platform from different views and standoff distances.

The hexacopter requires a single operator to launch, fly a mission and recover the aircraft. However, the system is also designed to allow one operator to fly the aircraft in manual mode, while another operator commands the aircraft through a computer-based Ground Control Station (GCS). The GCS software used in this study is called Mission Planner (3D Robotics, Inc.). Utilising GCS provided a command and control interface with the Ptarmigan and helped to calibrate and configure the autopilot, plan and save mission data, and view live data in flight. The same command link configuration enables the second operator to fully control the imaging device. This allows the primary operator to concentrate on safety of flight by focusing only on control of the aircraft and not the imaging device.

2.3. Mission and UAV flight planning

With respect to the final image-based 3D reconstruction, there are many image capture factors that directly impact model accuracy, resolution, and completeness. These include: the configuration of image acquisition in terms of camera positioning, the number of captured images, adjacent image overlapping and image quality. In order to satisfy the accuracy demands with respect to the bridge geometry, thorough flight path planning was done prior to each flight. In this work, images were captured in a series of imaging flight paths. Each path was designed to capture and reconstruct aspects of the targeted bridge at a variety of length scales (analogous to pixel size), ranging from the overall geometry to fine-scale details of critical regions of interest.

The images were captured such that each part of an aspect of interest was covered by multiple images arranged in overlapping strips to ensure full redundant coverage. Throughout the project, an overlap percentage of 90% in the horizontal direction and 60% in the vertical direction was specified. The distance between the UAV platform and bridge was influenced by factors including the camera field of view, sensor resolution, and the safety of aircraft. A total of 22 flight paths were designed to capture more than 2000 high-resolution images from the bridge at eight different distances from the bridge itself. These flight paths were planned

with the UAV ground control station, but the actual piloting was performed via the UAV remote control radio link with an observer on the opposite bank providing guidance to the UAV pilot. This guidance by the observer was by radio and arm/hand gestures to help steer the UAV, maintain a safe standoff distance from the bridge, and to let the pilot know when to stop the flight in one direction and return to the opposite shore on the next planned flight line (Figure 3).

Mission protocols dictated that the UAV not be flown through the interior of the truss, out of concern for the UAV. Images for this region on the bridge were captured by an inspector using a Nikon D800E (36.3-megapixel resolution) camera with Nikon Nikkor AF-S 50 mm and Micro-Nikkor 105 mm lenses. The point clouds generated from these images were merged with those captured via UAV to complement the point cloud model, as will be described herein.

2.4. Point cloud generation process

The image-based 3D point clouds were generated using an adaptation of a DSfM process referred to as Hierarchical Point Cloud Generation (HPCG). The details of the HPCG process are beyond the scope of this work, and the reader is referred to Khaloo and Lattanzi (2016) for more details. An overview of the process follows.

Images of a bridge are first captured at several pixel sizes, corresponding to the standoff distance of the UAV from the bridge. These images are then used to generate a series of 3D point clouds at different length scales using DSfM, resulting in a separate point clouds for each captured set of images. The reconstruction starts with Structure-from-Motion (SfM), which simultaneously determines camera parameters (also known as the camera 'pose') and the 3D spatial location of points in the images, producing sparse and non-photorealistic 3D point clouds incrementally.

The first step in SfM is to extract salient feature descriptors such as the Scale Invariant Feature Transform (SIFT) (Lowe, 2004), Binary Robust Invariant Scalable Keypoint (BRISK) (Leutenegger, Chli, & Siegwart, 2011) or Speed-Up Robust

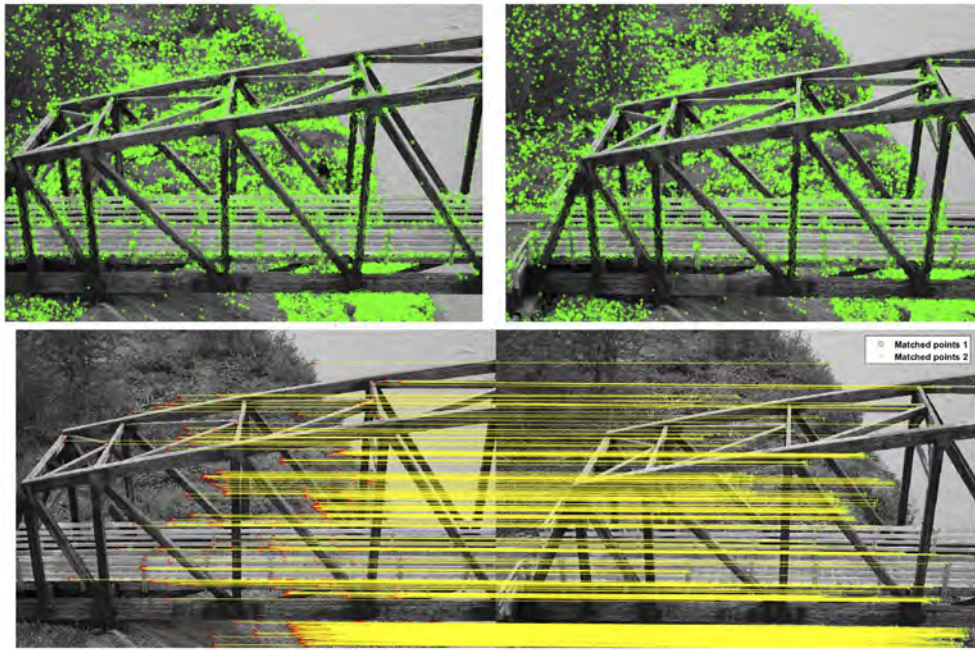


Figure 4. SIFT feature detection (top) and feature matching between two adjacent views (bottom) For clarity, only 400 out of 1823 matched features are shown.

Features (SURF) (Bay, Ess, Tuytelaars, & Van Gool, 2008) for feature extraction within each 2D image. Since automated image-based modelling methods rely on these extracted features, occlusions, illumination changes, limited access for image acquisition and poorly textured surfaces can be problematic. As one of the most comprehensive and robust algorithms with respect to these challenges, the SIFT method was utilised in this study due to its consistently superior performance in 3D point cloud reconstruction, also investigated by Bae, White, Golparvar-Fard, Pan, and Sun (2015).

Once features have been detected throughout the data-set, the features are matched across an image pair using the multithreaded implementation of the Fast Approximate Nearest Neighbours (FANN) algorithm (Muja & Lowe, 2014). Using Exchangeable Image Format (EXIF) metadata embedded in each digital image to extract values of the focal length and image size, a fundamental matrix (*F-matrix*) (Hartley & Zisserman, 2004) is fitted to all the features in the image pair based on the epipolar geometry, in tandem with RANSAC (RANDOM SAMPLE CONSENSUS) (Fischler & Bolles, 1981) and the eight-point algorithm to remove outliers and false matches (Hartley & Zisserman, 2004). To illustrate, Figure 4 shows the extracted and matched SIFT feature points on sample images from Placer River Bridge.

An initial image pair with optimal overlap and intersection geometry is then selected to initiate the sparse 3D reconstruction process. Once an image pair is selected, the relative orientation between these two images and camera parameters is then determined by using the five-point algorithm (Nistér, 2004) followed by a triangulation into 3D points and Bundle adjustment error minimisation (Lourakis & Argyros, 2009).

Subsequently, new images are added by estimating the camera pose from correspondences between 3D points and image features using the Perspective-*n*-Point (PnP) algorithm (Lepetit, Moreno-Noguer, & Fua, 2009) in a M-estimator SAMple Consensus (MSAC) (Torr & Zisserman, 2000) procedure. This

process is iterated until a camera pose is determined for all images. A sparse 3D point cloud is then generated, using the camera poses to project the features into a 3D space. Global Bundle adjustment is used to refine the results and minimise error at the end of each iteration. In this work, Agisoft Photoscan (2016) computer software was used to register images and generate sparse 3D point clouds.

Each sparse point cloud is then transformed into a dense 3D point cloud using a global pixel-wise image-matching algorithm known as Semi-global Matching (SGM) (Hirschmuller, 2008). In this context, the *dense* term refers to the procedure of capturing information from all pixels in the input 2D image. This is in contrast to sparse methods, where only extracted feature points are considered.

The utilised SGM algorithm is based on an energy function minimisation along the eight possible directions for a given pixel in an image (i.e. every 45°). The energy function includes a pixel-matching cost function, C , which accounts for the similarity level of two pixels in an image pair, p and q , along with two constraints, P_1 and P_2 , which cope with possible errors in the SGM algorithm and compensate radiometric differences between input images. The pixel-wise cost and the smoothness constraints are expressed by defining the energy $E(D)$ that depends on the depth map image D (Hirschmuller, 2008):

$$E(D) = \sum_p \left(C(p, D_p) + \sum_{q \in N_p} P_1 T[|D_p - D_q| = 1] + \sum_{q \in N_p} P_2 T[|D_p - D_q| > 1] \right) \quad (1)$$

In this context, disparity (depth map) refers to the difference in position between the projections of a 3D point in an image pair (Szeliski, 2011). The first term in Equation (1) is the sum of all pixel-matching costs for the disparities of D . The second term adds a constant penalty P_1 for all pixels q in the neighbourhood

N_p of p , for which the disparity changes at most 1 pixel. The third term adds a larger constant penalty, P_2 , for all larger disparity changes (e.g. discontinuities). Utilising a lower penalty, P_1 , for small changes permits an adaptation to slanted or curved surfaces (Hirschmuller, 2008). Within Equation (1), T is a binary operator evaluating to one if the subsequent condition is true and evaluates to zero otherwise.

In this work, SURE (SURface REconstruction from imagery) (Rothermel, Wenzel, Fritsch, & Haala, 2012) was used, which implements an adaptation of the SGM algorithm that reduces processing time with low memory consumption (Rothermel et al., 2012). SURE utilises the full resolution of images and the corresponding camera orientation parameters estimated at the sparse reconstruction phase to derive up to one 3D point per pixel by utilising a fusion method based on geometric constraints. The high redundancy resulting from multiple disparity maps sharing the same reference view was later used to increase precision through outlier and mismatch elimination within a fusion step. Therefore, two criteria were applied within the dense reconstruction procedure: (i) maximum reprojection error of 0.3 and (ii) rejection of measurements with very small intersection angles (below 4°).

The separate point clouds for each image set are then globally registered and merged together into a unique final 3D model using a robust variant of the Iterative-Closest-Point (ICP) algorithm (Toldo, Beinat, & Crosilla, 2010). ICP starts with two 3D point clouds and an initial guess for their relative rigid-body transform, and iteratively refines the transform by minimising an error function based on the sum of squared distances. Later, since the absolute distances between camera poses are not available, the scale-free image-based reconstructed point clouds were properly scaled using dimensioned reference lengths collected on-site.

Utilising tightly integrated UAV flight path planning in tandem with the HPCG approach avoids the inherent difficulties of registering camera images with broadly varying pixel scales. By creating individual clouds at each pixel scale (UAV stand-off distance) and then merging, the practical result of this approach is that small-scale features such as timber shakes and splits can be consistently represented in a 3D point cloud of the entire bridge.

2.5. Evaluative metrics

The results of the inspection were evaluated in a variety of ways, both qualitative and quantitative. During the construction of the bridge, fabrication and construction errors initiated a series of minor defects in the bridge. These defects were identified early on in the process as representative of the kinds of details that must be tracked and assessed during the NBIS inspection process. In this work, they were used to provide illustrative and qualitative assessments of the capabilities of the UAV-based inspection approach to capture and represent structural details with sufficient accuracy for NBIS purposes.

Quantitatively, the UAV-captured point cloud was compared against a point cloud constructed using Faro Focus^{3D} phased shift-based LIDAR system. LIDAR is a well-established polar measurement system that directly generates 3D point clouds of the targeted structure. Laser scanning represents an alternative potential technology for USFS, as it is capable of generating

high-quality 3D point cloud models of structures. The quality and accuracy of the image-based 3D point clouds were compared against the LIDAR model using metrics to evaluate these generated 3D models on a local (per-point) basis. Two metrics were used to assess each reconstruction method through extracting 3D geometric features: (i) local noise level and (ii) local point density of 3D point clouds. While local noise level examines the global accuracy of the 3D model generation, point density can be used to compare the resolution of these models.

The local noise level in a 3D point cloud can be estimated based on the residual between each point and the best fitting plane computed on its local nearest neighbours. Noise, nonconformity of the neighbourhood of a point, imperfect data registration and variations in the physical texture of the reconstructed scene (from smooth to highly irregular surfaces) can all affect this residual value.

In order to efficiently determine the local nearest neighbours for every point in the data-set, the space partitioning method called k - d trees was applied to the well-known k -Nearest Neighbours (k -NN) algorithm to reduce the search complexity. Utilising k -NN rather than a Fixed Distance Neighbourhood (FDN) avoided the problem of point density variation within point clouds (Hoppe, DeRose, Duchamp, McDonald, & Stuetzle, 1992). For the k points that form the neighbourhood of a 3D point p_i in a point cloud, the covariance matrix, \mathbf{C} , is defined as (Jolliffe, 2002):

$$\mathbf{C}_{3 \times 3} = \frac{1}{k} \sum_{i=1}^k (p_i - \bar{p})(p_i - \bar{p})^T; \bar{p} = \frac{1}{k} \sum_{i=1}^k p_i \quad (2)$$

where \bar{p} is the local data centroid (arithmetic mean) within p_i 's neighbourhood (N_{p_i}).

Throughout this study a value of $k = 50$ points was assigned in order to achieve a sufficiently large and robust neighbourhood to quantify noise while still reflecting local surface properties. Using Singular Value Decomposition (SVD) (Golub & Reinsch, 1970), the covariance matrix is then decomposed into eigenvalues $\lambda (\lambda_2 \geq \lambda_1 \geq \lambda_0)$ and $\mathbf{V} (v_2, v_1 \text{ and } v_0)$ eigenvectors. Since \mathbf{C} is symmetric and positive semi-definite, all eigenvalues λ are real-valued and the eigenvectors \mathbf{V} form an orthogonal frame, corresponding to the principal components of the point set defined by the k -Nearest Neighbours (k -NN) of the 3D point p_i . Within this approach, v_0 approximates the point's p_i normal, while v_2 and v_1 span the local tangent plane. The utilised method gives an equivalent solution to the total least squares formalisation of the plane-fitting problem.

In addition, the lowest valued eigenvalue (λ_0) approximates the variation along the surface normal (v_0), which quantitatively describes the local noise level (a.k.a surface roughness) around each 3D point, i.e. how much the k points deviate from the best-fitted plane. If $\lambda_0 = 0$, then all the points within N_{p_i} lie in the perfect plane.

The quality of generated point clouds was also examined with respect to the local density of the points. To obtain an estimate of local density ρ at a point \mathbf{p} , where $\rho = \frac{k+1}{\frac{4}{3}\pi r_{k-NN}^3}$ and r_{k-NN} is the radius of the spherical neighbourhood of the k closest neighbours of a 3D point \mathbf{p} given:

$$r_{k-NN} = \max_{i \in N_p} \|p - p_i\| \quad (3)$$

Table 2. Data collected during field testing.

Data type	Sensor type	No. Images/ Videos/Scans	Size (GB)	Notes
Digital image	Sony NEX-7	2626	24.7	Captured by UAV
Digital image	Nikon D800E	2222	34.9	Captured by inspector
Video	GoPro Hero 3	20	7.6	Captured by UAV
Point cloud	FARO Focus ^{3D}	12	4.3	Captured by inspector

where r_{k-NN} represents the distance from the point of interest to the furthest neighbor. This approach provides a unique estimate of the local point density for all the points in a 3D data-set in a fast and simple manner. In this study in order to calculate the number of points inside a sphere centered on each point \mathbf{p} , r_{k-NN} was set to 0.62 m to achieve an enclosing volume of 1 m^3 .

3. Results

The two-day mission took place on 9 and 10 June 2015. Two pilots performed the flights, with one pilot acting as observer to prevent the UAV pilot from endangering the UAV while flying near the river and/or while under the bridge. A variety of calibration and test flights preceded the inspection flights. Because the bridge and river are situated in a valley, there were times when mountains blocked views of the Global Positioning System (GPS) satellite, thus optimal GPS satellite geometry was not consistently available. A good GPS horizontal dilution of precision (HDOP) of less than 2.4 was specified for aircraft launch, flight, and recovery throughout this mission.

Data were collected via both UAV cameras and the human-controlled camera. The GoPro captured images of the underside of the deck, while the Sony NEX-7 was programmed to capture still images every second. Unfortunately, the minimal exposure controls on the GoPro in conjunction with the high visual contrast between the deck underside and the sky led to underexposed images that were not useable for image-based modelling. The images captured by the human inspector were taken from the bridge deck, without any ladders or climbing

aids. Effectively, the exterior of the truss was modelled via UAV-acquired images and the interior of the truss was modelled with human-captured images. In order to maximise the benefits from both of these image capturing strategies, these image-based models were globally registered and merged together to create a single *hybrid* 3D model.

As discussed in more details in Khaloo and Lattanzi (2016), in order to minimise the accumulative errors in the pair-wise registration of large-scale point clouds, Generalized Procrustes Analysis (GPA) was embedded into an ICP computation for merging the clouds (Toldo et al., 2010). As indicated, a compilation of LIDAR scans of the bridge was also captured for comparative purposes. These scans captured both the interior and exterior of the truss structure. A complete list of the data collected during the inspection mission is shown in Table 2.

3.1. 3D modelling: comparative results

Renderings of the LIDAR and HPCG generated 3D point clouds are shown in Figures 5 and 6, respectively. From the rendered viewpoint, there is not much to distinguish the quality of the two models. A comparison of the model characteristics is more indicative. As illustrated in Figures 7 and 8, the noise characteristics are very different between these two 3D reconstruction techniques. The LIDAR scanner produced a rather consistent precision and very low noise model with a mean estimated roughness value of 1.8 mm.

However, due to imperfect correspondence between 3D point clouds, higher local noise was consequently introduced into the final model within the registration process of multiple scans. As shown in Figure 7, the positions of different scanning locations become apparent by the increase in noise around them. Furthermore, as discussed later, the resolution of the LIDAR point cloud was limited and unsatisfactory due to the minimum acquisition distance and restricted depth precision.

The image-based 3D reconstruction exhibited noise that was one to two greater orders of magnitude, based on the calculated roughness values (Table 3). This increase in noise can be attributed in part to fundamental differences in 3D reconstruction methods, as the DSfM process typically exhibits increased noise

**Figure 5.** The Placer River Bridge 3D LIDAR-based model.



Figure 6. The Placer River Bridge 3D HPCG-based model (only using UAV-acquired images).

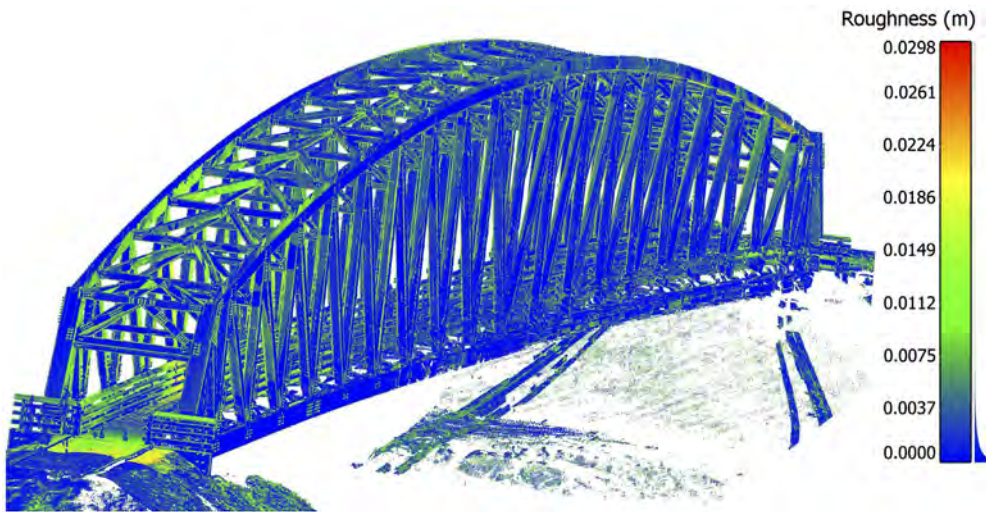


Figure 7. Local noise level for LIDAR-based point cloud model.

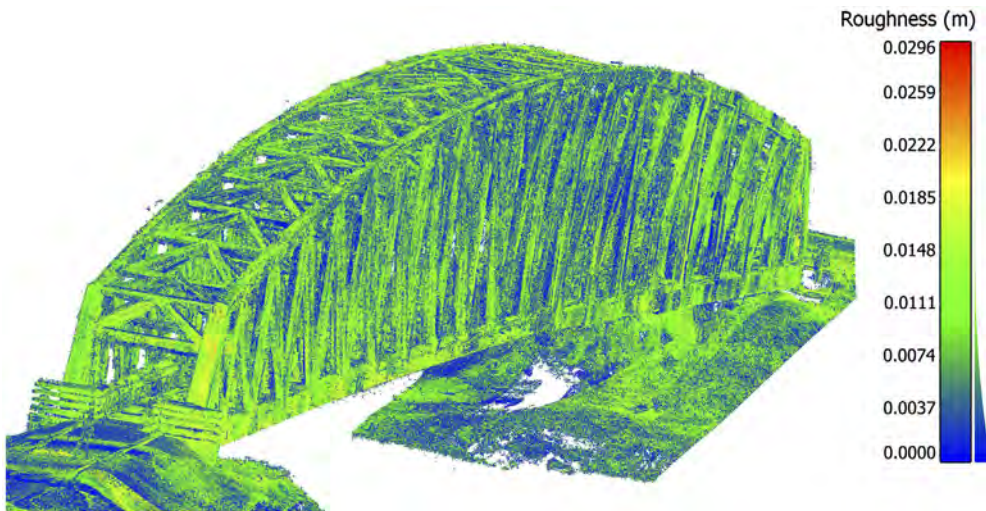


Figure 8. Local noise level for 3D HPCG-based model (only using UAV-acquired images).

relative to LIDAR (Khaloo & Lattanzi, 2015). In large part, this increased noise was also due to the complex interactions of the bridge with the low contrast sky that was in the background of many captured images, highlighting the impact of environmental

and radiometric (e.g. surface reflectivity and texture) factors on the quality of the image-based reconstruction. The increase in local noise is also result of the relation between the distance of two adjacent camera locations and the actual distance between

Table 3. Resolution and noise level comparison.

Reconstruction methods	Number of points	Local point density (points/m ³)	Noise level (mm)
LIDAR	202,790,259	1,478,099	1.8
Image-based UAV	710,920,835	2,258,516	4.8
Image-based hybrid	1,412,060,890	5,656,185	4.5

the camera and the object of interest (also known as base-to-depth ratio). Since a large number of images were captured with a relatively small base-to-depth ratio, an increase in the depth estimation error caused higher local noise levels.

Comparisons of the 3D model of the bridge generated using only UAV-acquired images with the model that combines UAV and human inspector captured data-set (hybrid model) reflected little change (close to 0.3 mm) in the point cloud noise, though with double the number of points, indicating that the UAV imaging platform itself did not induce additional noise in the reconstruction.

Table 3 also provides a comparison of the total number of points and the local point density for each reconstruction. The point cloud model generated solely from UAV-acquired images, which only captured images of the truss exterior, had 3.5 times as many points as the LIDAR system that captured the interior of

the truss structure as well. Including the human-captured images of the truss interior (hybrid model) doubled the total number of points. This increase in the number of points, and consequently the higher density, is analogous to an increase in image resolution and total number of pixels processed that directly impacted the ability to resolve and assess details captured in the final complete 3D model.

3.2. 3D modelling: representation of bridge details

In terms of the deficiencies and damages that are visually observable, several exemplar cases were examined. Comparisons of damages captured in field images and renderings from the hybrid point cloud are provided in Figures 9–11. For all of the damaged regions (DR), the rendering of the flaw is clear and photorealistic. Some noise can be observed around the exterior of the truss chords (DR 2), but this does not impede observation of the structural elements themselves. There are some minor visual artefacts in the rendering of the loose connection (DR 3) due to shadows cast by the bolt itself (Figure 11).

Comparisons of how details were rendered in the LIDAR and image-based hybrid point clouds are shown in Figures 12 and 13. Near the abutments, where it was possible to place the LIDAR scanner near the bridge, a dense and reasonably photorealistic model is generated, though the LIDAR model is less dense than

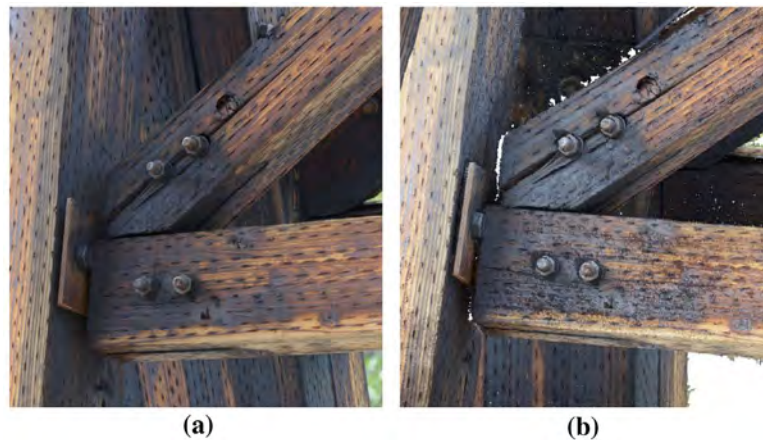
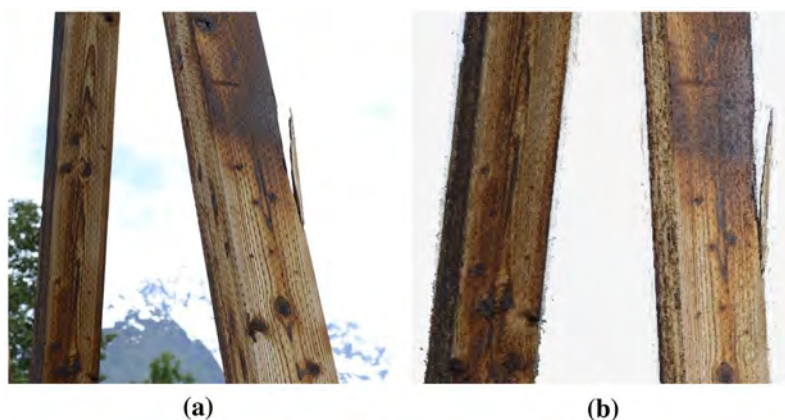
**Figure 9.** Connection damage on west truss – DR 1 (a). field image (b). HPCG-based hybrid 3D point cloud rendering.**Figure 10.** Damaged truss chord on east truss – DR 2 (a). field image (b). HPCG-based hybrid 3D point cloud rendering.



Figure 11. Loose bolt on west truss – DR 3 (a). field image (b). HPCG-based hybrid 3D point cloud rendering.

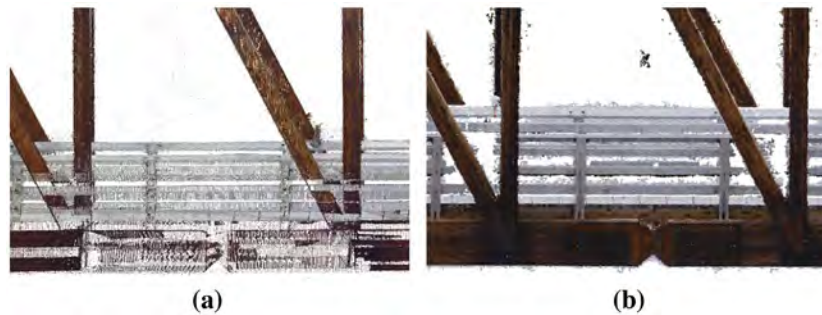


Figure 12. Rendering of mid-span hinge (a). LIDAR model (b). HPCG-based hybrid 3D point cloud.

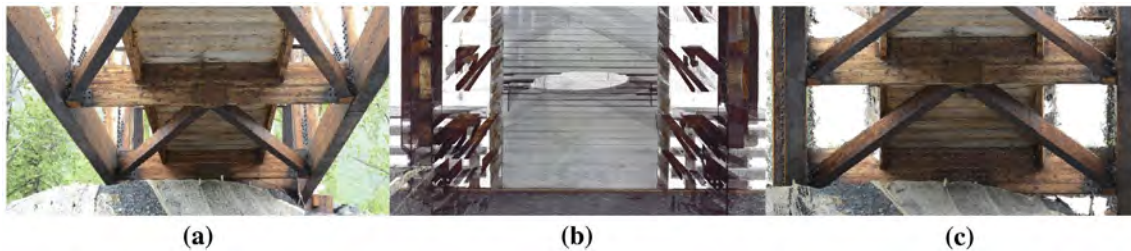


Figure 13. Rendering of underside of the bridge deck on western abutment (a). field image (b). 3D LIDAR model (c) HPCG-based hybrid 3D point cloud.

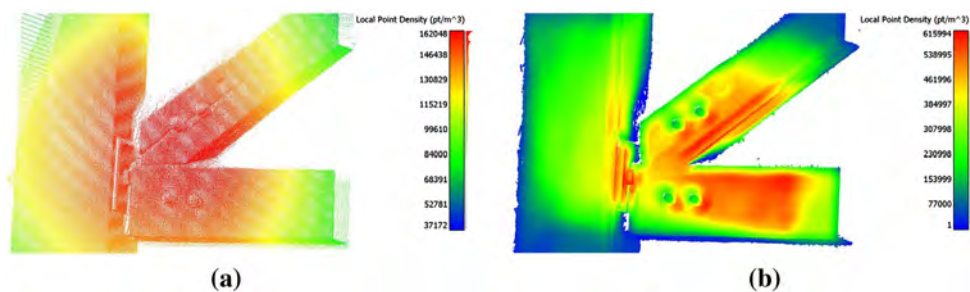


Figure 14. Local point cloud density of connection damage on west truss (a). LIDAR model (b). HPCG-based hybrid model.

the UAV-based model. Note the reduced noise when compared to the UAV generated model as well. However, when the renderings of the mid-span hinge are compared, the differences in the reconstruction approaches become apparent. For the hinge, the closest the scanner could be placed was approximately 50 m away. The LIDAR point cloud at this distance is so sparse as to

be effectively useless for the purposes of structural assessment. The UAV-generated model clearly renders the bolt patterns and gusset plates.

Figure 13 provides visual comparison of different 3D point clouds under the deck of the bridge. As with the LIDAR model, the low-point density due to limited scanning position results

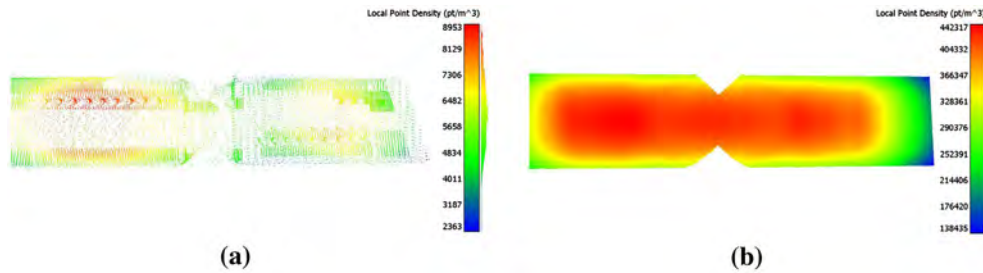


Figure 15. Local density at mid-span hinge (a). LIDAR models (b). HPCG-based hybrid model.

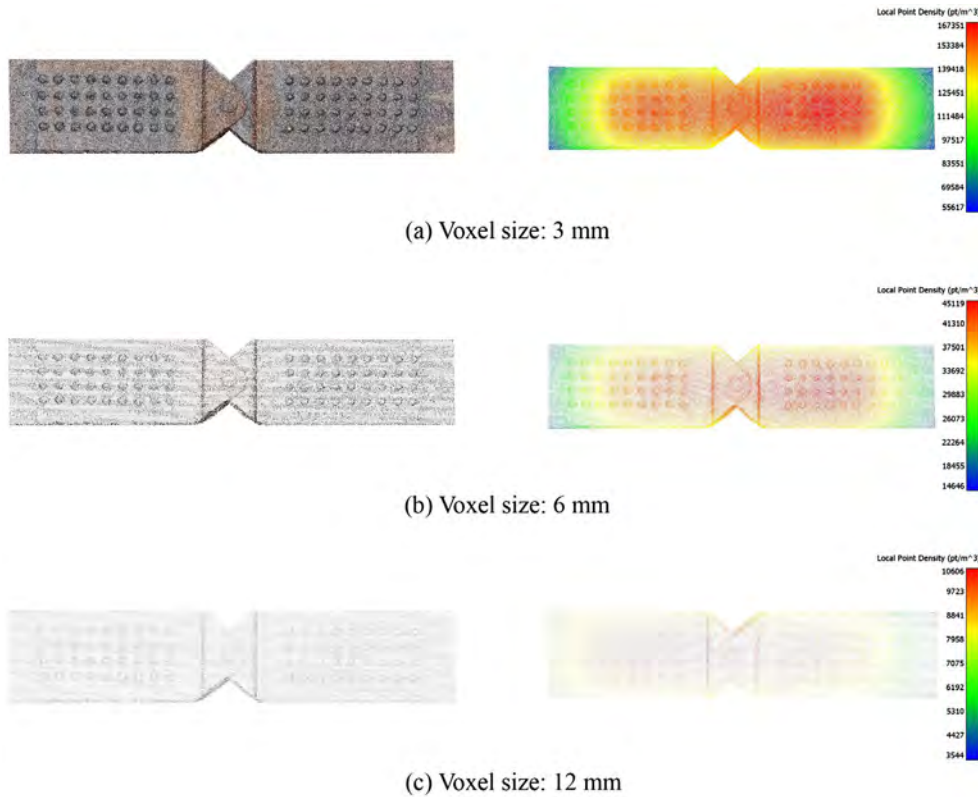


Figure 16. Downsampled representations of the mid-span hinge 3D model using different voxel sizes.

in missing data and lack of resolution. In contrast, the more flexible nature of UAV imaging provided a more accurate and complete dense 3D model. The estimated local density, presented in Figures 14 and 15, further illustrates the characteristics of the hybrid model relative to the LIDAR system.

What this comparative study suggests is that LIDAR could effectively generate point cloud models for inspection purposes when it was possible to place the scanner near the structure, though there was a trade-off in model resolution for improvements in model noise characteristics. The resolution of the LIDAR model was controlled by the angular resolution of the system, while the precision of the points was mainly defined by laser measurement precision, leading to a relatively homogeneous model with consistent precision over a large range.

However, there were significant drawbacks to using LIDAR in this inspection scenario. The LIDAR scanner could only be placed on level and stable terrain, which inhibited the scanning of some regions of the bridge, particularly the mid-span of the

bridge, but also underneath the abutments. Furthermore, in order to generate a complete 3D model of the bridge, many scanning positions were needed, which made on-site data capture time consuming. Lastly, and most critically, the polar nature of the scan density dictated that regions of the bridge farther from the location of the scanner were reconstructed with lower resolution.

Neglecting noise, the DSfM models had orders of magnitude more resolution, resulting in more photorealistic and useable point cloud data. Beside higher geometrical resolution, denser colour information was available, improving the visualisation of the resulting 3D point cloud model (Figures 5 and 6), and leading to improved interpretive capabilities for inspection. Most importantly, the true value of the UAV inspection system was the ability to accurately reconstruct details in regions where it was not possible to set up a LIDAR scanner within reasonable proximity (Figure 15). The integrated UAV flight path planning and photogrammetric reconstruction system allowed for more flexible data acquisition, particularly for difficult to access regions

of a bridge. When compared to LIDAR, the trade-offs for these improvements were increased post-processing and computational effort, as well as increased point cloud noise.

For the mid-span hinge illustrated in Figure 15, the image-based 3D model contains 1,230,478 points, an almost 60 times higher geometric resolution than the data acquired from LIDAR. The average local point cloud density value for each of these data-sets was 358,933 (point/m³) and 6137 (point/m³), respectively. Distance between the scanning locations and the object of interest along with angle of incidence and surface reflectivity, all result in lower density in the LIDAR model.

Furthermore, to investigate the required point density needed to assess the structural integrity, the image-based 3D model of the mid-span hinge connection was uniformly downsampled by using an octree approach to sub-divide the data-set into a set of cubical regions (also known as 3D voxel grids), then taking the spatial centroid (average point inside a voxel) to downsample the data-set. Within the voxelisation step, three voxel sizes ($d = 3, 6$ and 12 mm), were considered in order to produce point clouds with different spatial resolutions. Each resulting subsampled model contains 404,753 points (mean local density = 135,514 pt/m³), 108,846 points (mean local density = 36,632 pt/m³) and 25,797 points (mean local density = 8632 pt/m³), respectively.

Figure 16 depicts the effect of the local density on the level of detail that can be resolved in the 3D point clouds. As expected, downsampling clearly degraded the ability to visualise high fidelity details on the hinge. The loss of geometric resolution along with colour information would have direct impact on the ability to utilise this data for visual inspection purposes. As shown in Figure 16(b), models with an average point density of less than 50,000 pt/m³ on each element of the structure proved insufficient for developing models photorealistic enough to conduct visual damage assessments.

4. Conclusions

In this study, it has been shown that utilising a data-driven approach for designing the UAV platform and acquisition of 2D digital images in conjunction with a modern 3D scene reconstruction technique can effectively facilitate and augment the inspection and evaluation of large-scale infrastructure systems such as bridges. By leveraging the flexible nature of UAV image data collection and thorough flight path planning, it was possible to acquire images from all possible points of view, overcoming limited inspection accessibility and occlusions. This approach provided the completeness and accuracy needed for both detailed 3D in-situ modelling and structural condition assessment. In addition, the presented approach outperformed LIDAR in terms of completeness and resolution.

Several environmental factors were observed to impact the results of these test flights and quality of the final 3D reconstruction. The lack of vegetation around the structure permitted adequate clearance for operation of the UAV and LIDAR scanner. As planted shrubs mature, they will obscure the structure and impede imaging. The contrast of the underside of the deck and the overcast sky made proper image exposure a challenge, notably for the GoPro, which did not have adequate manual exposure controls. Lastly, the low-texture, overcast sky effectively induced noise into the image-based 3D point cloud

models due to inaccurate point correspondences. The developed reconstruction process mitigated this issue to some degree, as compensation for radiometric differences of input images was accounted for in the dense reconstruction algorithm.

Overall, the designed inspection process and subsequent results showed that UAV can provide valuable sources of information to support the NBIS inspection process. The use of a UAV minimises time on site and increases safety by removing potential points of failure such as suspended platforms, ladders, and harnesses used in conventional inspection techniques. There remains a need for safety protocols for operating UAV near the travelling public, an issue that was not considered in this study due to the remote location and lack of visitors during the test flights. Standardisation of the mission planning and data analysis processes are needed as well if UAV inspections are to become an integrated part of the NBIS process.

With the newly issued Federal Aviation Regulations – Part 107 (Federal Aviation Administration [FAA], 2016), which covers a broad range of usage for UAVs weighing less than 25 kg, operations can be conducted outdoors under specified operational and safety regulations. It is anticipated that these new regulations will help standardise workflows in order to leverage UAV and visual data analytics in civil infrastructure condition assessment.

Another avenue for future work is in studying the method presented here when compared against rotary UAV platforms equipped with high accuracy (± 1 cm) advanced LIDAR sensors. While the development of such UAV systems and sensors is still an open area of research, particularly considering that fixed wing UAV are not well suited to the bridge inspection environment, advancements in this domain are emerging rapidly. Such systems would address many of the challenges with the terrestrial LIDAR system used in this work and are likely to eventually provide a comparable alternative to UAVs that utilise photogrammetric methods.

The project team intends to repeat the developed inspection process at the Placer River site in the next couple of years. The 3D virtual model results from this repeat inspection will then be directly compared through computer vision-based and point cloud analysis techniques to track how critical details are changing over the life-cycle of the bridge. Performance changes such as differential camber sag will also be evaluated using these methods. In order to enable this long-term monitoring, replicable UAV inspection methods and protocols are vital, as they will ultimately facilitate the high quality and sufficiently comparable point cloud models.

Acknowledgements

Any opinions, findings, and conclusions or recommendations expressed in this publication are those of the authors and do not necessarily reflect the views of the U.S. Forest Service.

Disclosure statement

In accordance with Taylor & Francis policy and our ethical obligation as researchers, we, Ali Khaloo and David Lattanzi, are reporting that we have a business interest in a company that may be affected by the research reported in the enclosed paper. We have disclosed those interests fully to Taylor & Francis, and have in place an approved plan for managing any potential conflicts arising from that involvement.

Funding

This material is based in part upon work supported by the U.S. Forest Service [grant number 15-CS-11100100-015].

ORCID

David Lattanzi  <http://orcid.org/0000-0001-9247-0680>

References

- Agisoft PhotoScan. (2016). *Professional edition – version 1.1.6*. St. Petersburg: Agisoft LLC.
- Bae, H., White, J., Golparvar-Fard, M., Pan, Y., & Sun, Y. (2015). Fast and scalable 3D cyber-physical modeling for high-precision mobile augmented reality systems. *Personal and Ubiquitous Computing*, 19(8). doi:10.1007/s00779-015-0892-6
- Bay, H., Ess, A., Tuytelaars, T., & Van Gool, L. (2008). Speeded-Up Robust Features (SURF). *Computer Vision and Image Understanding*, 110, 346–359. doi:10.1016/j.cviu.2007.09.014
- Colomina, I., & Molina, P. (2014). Unmanned aerial systems for photogrammetry and remote sensing: A review. *ISPRS Journal of Photogrammetry and Remote Sensing*, 92, 79–97. doi:10.1016/j.isprsjprs.2014.02.013
- Díaz-Vilariño, L., González-Jorge, H., Martínez-Sánchez, J., Bueno, M., & Arias, P. (2016). Determining the limits of unmanned aerial photogrammetry for the evaluation of road runoff. *Measurement*, 85, 132–141. doi:10.1016/j.measurement.2016.02.030
- Ellenberg, A., Kotsos, A., Moon, F., & Bartoli, I. (2016). Bridge related damage quantification using unmanned aerial vehicle imagery. *Structural Control and Health Monitoring*, 23, 1168–1179. doi:10.1002/stc.1831
- Federal Aviation Administration. (2016). *Fact sheet – Small unmanned aircraft regulations* (Part 107). Washington, DC: Federal Aviation Administration of the USDOT. Retrieved from https://www.faa.gov/news/fact_sheets/news_story.cfm?newsId=20516
- Fernandez Galarreta, J., Kerle, N., & Gerke, M. (2015). UAV-based urban structural damage assessment using object-based image analysis and semantic reasoning. *Natural Hazards and Earth System Sciences*, 15, 1087–1101. doi:10.5194/nhess-15-1087-2015
- Fischler, M. A., & Bolles, R. C. (1981). Random sample consensus: A paradigm for model fitting with applications to image analysis and automated cartography. *Communications of the ACM*, 24, 381–395. doi:10.1145/358669.358692
- Golub, G. H., & Reinsch, C. (1970). Singular value decomposition and least squares solutions. *Numerische Mathematik*, 14, 403–420. doi:10.1007/BF02163027
- Hartley, R., & Zisserman, A. (2004). *Multiple view geometry in computer vision*. (2nd ed.). Cambridge: Cambridge University Press.
- Hirschmuller, H. (2008). Stereo processing by semiglobal matching and mutual information. *IEEE Transactions on Pattern Analysis and Machine Intelligence*, 30, 328–341. doi:10.1109/TPAMI.2007.1166
- Hoppe, H., DeRose, T., Duchamp, T., McDonald, J., & Stuetzle, W. (1992). *Surface reconstruction from unorganized points*. Proceedings of the 19th Annual Conference on Computer Graphics and Interactive Techniques (SIGGRAPH), New York, NY, USA, pp. 71–78. doi:10.1145/133994.134011
- Jahanshahi, M. R., Kelly, J. S., Masri, S. F., & Sukhatme, G. S. (2009). A survey and evaluation of promising approaches for automatic image-based defect detection of bridge structures. *Structure and Infrastructure Engineering*, 5, 455–486.
- Jolliffe, I. (2002). *Principal component analysis*. Hoboken, NJ: John Wiley & Sons.
- Khaloo, A., & Lattanzi, D. (2015). *Extracting structural models through computer vision*. Paper presented at the Structures Congress, Portland, OR, pp. 538–548. doi:10.1061/9780784479117.047
- Khaloo, A., & Lattanzi, D. (2016). Hierarchical dense structure-from-motion reconstructions for infrastructure condition assessment. *Journal of Computing in Civil Engineering*, 31, 4016047. doi:10.1061/(ASCE)CP.1943-5487.0000616
- Lattanzi, D., & Miller, G. (2015). 3D scene reconstruction for robotic bridge inspection. *Journal of Infrastructure Systems*, 21, 4014041. doi:10.1061/(ASCE)IS.1943-555X.0000229
- Lepetit, V., Moreno-Noguer, F., & Fua, P. (2009). EPnP: An accurate O(n) solution to the PnP problem. *International Journal of Computer Vision*, 81, 155–166. doi:10.1007/s11263-008-0152-6
- Leutenegger, S., Chli, M., & Siegwart, R. Y. (2011). *BRISK: Binary robust invariant scalable keypoints*. Paper presented at the computer vision (ICCV), IEEE International Conference, Barcelona, Spain.
- Lourakis, M. I. A. & Argyros, A. A. (2009). SBA: A software package for generic sparse bundle adjustment. *ACM Transactions on Mathematical Software*, 36, 2:1–2:30. doi:10.1145/1486525.1486527
- Lowe, D. G. (2004). Distinctive image features from scale-invariant keypoints. *International Journal of Computer Vision*, 60, 91–110. doi:10.1023/B:VISI.0000029664.99615.94
- Mascareñas, D., Flynn, E., Farrar, C., Park, G., & Todd, M. (2009). A mobile host approach for wireless powering and interrogation of structural health monitoring sensor networks. *IEEE Sensors Journal*, 9, 1719–1726.
- McGuire, B., Atadero, R., Clevenger, C., & Ozbek, M. (2016). Bridge information modeling for inspection and evaluation. *Journal of Bridge Engineering*, 21, 4015076. doi:10.1061/(ASCE)BE.1943-5592.0000850
- Metni, N., & Hamel, T. (2007). A UAV for bridge inspection: Visual servoing control law with orientation limits. *Automation in Construction*, 17, 3–10. doi:10.1016/j.autcon.2006.12.010
- Mission Planner (version 1.3) [Computer software]. Berkeley, CA: 3D Robotics.
- Muja, M., & Lowe, D. G. (2014). Scalable nearest neighbor algorithms for high dimensional data. *IEEE Transactions on Pattern Analysis and Machine Intelligence*, 36, 2227–2240. doi:10.1109/TPAMI.2014.2321376
- Murphy, R. R., Steimle, E., Griffin, C., Cullins, C., Hall, M., & Pratt, K. (2008). Cooperative use of unmanned sea surface and micro aerial vehicles at Hurricane Wilma. *Journal of Field Robotics*, 25, 164–180.
- Nistér, D. (2004). An efficient solution to the five-point relative pose problem. *IEEE Transactions on Pattern Analysis and Machine Intelligence*, 26, 756–770. doi:10.1109/TPAMI.2004.17
- Pajares, G. (2015). Overview and current status of remote sensing applications based on Unmanned Aerial Vehicles (UAVs). *Photogrammetric Engineering & Remote Sensing*, 81, 281–330. doi:10.14358/PERS.81.4.281
- Roca, D., Lagüela, S., Díaz-Vilariño, L., Armesto, J., & Arias, P. (2013). Low-cost aerial unit for outdoor inspection of building façades. *Automation in Construction*, 36, 128–135. doi:10.1016/j.autcon.2013.08.020
- Rodriguez-Gonzalez, P., Gonzalez-Aguilera, D., Lopez-Jimenez, G., & Picon-Cabrera, I. (2014). Image-based modeling of built environment from an unmanned aerial system. *Automation in Construction*, 48, 44–52. doi:10.1016/j.autcon.2014.08.010
- Rothermel, M., Wenzel, K., Fritsch, D., & Haala, N. (2012). *SURE: Photogrammetric Surface Reconstruction from Imagery*. Paper presented at the low-cost three dimensional (LC3D) Workshop, Berlin, Germany, pp. 1–9.
- Ryan, T. W., Mann, E., Chill, Z., & Ott, B. (2012). *Bridge Inspector's Reference Manual (BIRM)* (Report No. FHWA NHI 12-049). Washington, DC: Federal Highway Administration.
- Sánchez-Aparicio, L. J., Riveiro, B., González-Aguilera, D., & Ramos, L. F. (2014). The combination of geomatic approaches and operational modal analysis to improve calibration of finite element models: A case of study in Saint Torcato Church (Guimarães, Portugal). *Construction and Building Materials*, 70, 118–129. doi:10.1016/j.conbuildmat.2014.07.106
- Siebert, S., & Teizer, J. (2014). Mobile 3D mapping for surveying earthwork projects using an Unmanned Aerial Vehicle (UAV) system. *Automation in Construction*, 41, 1–14. doi:10.1016/j.autcon.2014.01.004
- Szeliski, R. (2011). *Computer vision – algorithms and applications*. Berlin: Springer.
- Toldo, R., Beinat, A., & Crosilla, F. (2010). *Global registration of multiple point clouds embedding the generalized procrustes analysis into an ICP framework*. Paper presented at the 5th international symposium on three dimensional data processing, visualization and transmission (3DPVT), Paris, France, pp. 1–8.
- Torr, P. H. S., & Zisserman, A. (2000). MLESAC: A new robust estimator with application to estimating image geometry. *Computer Vision and Image Understanding*, 78, 138–156. doi:10.1006/cviu.1999.0832